Science
AAAS

Supplementary Materials for

Multi-decadal trend of increasing iron stress in Southern Ocean phytoplankton

Thomas J. Ryan-Keogh[1*†], Sandy J. Thomalla[1,2†], Pedro M. S. Monteiro[1,2], Alessandro Tagliabue[3]

1. Southern Ocean Carbon-Climate Observatory, CSIR; Cape Town, 7700, South Africa

2. Marine and Antarctic Research for Innovation and Sustainability, University of Cape Town; Cape Town, 7700, South Africa

3. Department of Earth, Ocean and Ecological Sciences, School of Environmental Sciences, University of Liverpool; Liverpool, L69 3GP, UK

Correspondence to: tryankeogh@csir.co.za

This PDF file includes:

Materials and Methods

References (*62-86*)

Figs. S1 to S11

Tables S1 to S4

2

Materials and Methods

Data Selection and Download

BGC-Argo data, with synchronous iPAR profiles, from 47 floats were downloaded from the biogeochemical argo database (Table S3; https://biogeochemical-argo.org/), whilst ship-based data from 194 cruises were downloaded from various databases (Table S4) covering the Southern Ocean (Fig. 1A). Measurements were made across all months (Fig. S10A) from October 1996 to May 2022 (Fig. S10B). The initial database consisted of 9072 BGC-Argo profiles and 3934 ship-based profiles, with profiles excluded if not meeting quality control criteria (see NPQ and irradiance-normalised NPQ determination sections), resulting in a final database that consisted of 4129 BGC-Argo profiles and 1666 ship-based profiles (Fig. S10C). Southern Annular Mode data were retrieved from https://climatedataguide.ucar.edu/climate-data/. Core Argo mixed layer depth data were retrieved from http://mixedlayer.ucsd.edu/ (*62*). For sea surface temperature (SST) we used the Group for High Resolution Sea Surface Temperature (GHRSST; https://www.ghrsst.org/). Surface pH was taken from GLODAPv2021 (*63*). Ocean colour data were obtained from the ocean colour climate change initiative (https://esa-oceancolour-cci.org/; 58). Satellite derived photosynthetically active radiation data were retrieved from the merged GLOB colour project (http://www.globcolour.info/). Hadley EN 4.2.2 gridded temperature and salinity profiles (*64*) were converted to density and the MLD derived from a criterion of density of 0.03 kg m^{-3}. CMIP6 data were obtained from the Earth System Grid dataserver and includes depth integrated net primary production from the historical and SSP585 scenarios of the ACCESS, CESM2-WACCM, CESM2, CMCC-ESM2, CNRM-ESM2-1, CanESM5-CanOE, ED-Earth3-CC,

3

GFDL-ESM4, IPSL-CM6A-LR, MIROC-ES2L, MPI-ESM1-2-HR, MPI-ESM1-2-LR, MRI-ESM2-0M, NorESM2-LM, NorESM2-MM and UKESM1-0-LL models (*23*).

Profile Cleaning and Quenching Correction

Backscatter at 700 nm (b_{bp}, m^{-1}) was processed according to Schmechtig et al. (*65*) and the fluorescence (Flr: Ex/Em: 470 nm/695 nm) data were converted from raw digital counts to chlorophyll-a using half of the factory calibration slope (*66*). Ship-based data were only downloaded if Flr data, iPAR data and additional bio-optical data (b_{bp}, beam attenuation - c_p, or beam transmission - c_t) were available. In cases where only c_t (%) was provided the data were converted to c_p (m^{-1}) assuming a pathlength of 25 cm. In cases where only shipboard surface iPAR was available, depth profiles of iPAR were computed using K_d derived from the quenched Flr profiles following Kim et al. (*67*). Data from both BGC-Argo floats and ships were cleaned and despiked using an 11-point running median in accordance with Xing et al. (*68*) and an *in situ* dark correction was applied.

The Flr profiles were corrected for quenching using equations 10 and 11 from Xing et al. (*68*), where the quenching depth is defined as the depth of the max Flr:b_{bp} ratio (Flr:c_p) between the surface and whichever was shallowest of either the mixed layer depth (MLD) or the depth where *in situ* PAR (iPAR) is ~15 μmol photons m^{-2} s^{-1} (iPAR$_{15}$). The criterion for determining the MLD was based upon a density of 0.03 kg m^{-3} (*69*) as previously used for quenching correction methods (*68*, *70–72*). Below the quenching depth no correction is required, and above the quenching depth b_{bp} (c_p) is multiplied by the max Flr:b_{bp} (Flr:c_p) ratio.

4

NPQ and irradiance-normalised NPQ Determination

To determine the degree of NPQ, equation 5 of Ryan-Keogh & Thomalla (*38*) was applied as follows:

$$NPQ = \frac{(Flr_{QC} - Flr_Q)}{Flr_Q}$$

Where Flr_{QC} is the quenching corrected fluorescence profile and Flr_Q is the quenched fluorescence profile. Equation 3 of Ryan-Keogh & Thomalla (*38*) was applied to coincident profiles of NPQ and iPAR data to calculate α_{NPQ}, the light limited slope of NPQ (referred to as irradiance-normalised NPQ in the text), using a least-squares trust reflective region algorithm (*73*, *74*).

$$NPQ_{max} = NPQ \times (1 - e^{(-\alpha_{NPQ} \times (E/NPQ))})$$

Where E represents iPAR and NPQ_{max} represents the fitted maximum of NPQ. Values were excluded from further analysis if outside of the upper (1) and lower (0.002) bounds of the fitting procedure and if the root mean squared error (RMSE) was greater than the mean RMSE of the float deployment/cruise. To determine whether the use of b_{bp} or c_p made a difference in the estimation of α_{NPQ}, data from 6 cruises (Table S4: SANAE50, SANAE53, SANAE54, SANAE55, Winter2015, Winter2017) were compared (Fig. S11) and no significant differences were found (t-statistic = -0.37 – -0.04, p = 0.71 - 0.97, df = 29).

5

Net Primary Production Calculations

The following production models were used to calculate net primary production; the VGPM model (*48*) and the CbPM model (*49*), from both the BGC-Argo (2014 – 2021) data, with the additional CbPM model (*50*) and CAFE model (*51*) applied to remote sensing (1998 – 2021) data. OC-CCI remote sensing data (25 km, 9 day, v5.0) were used to calculate satellite net primary production, using PAR from the merged GLOB colour product. For the VGPM algorithm sea surface temperature (SST) was taken from as above. For the CbPM models and CAFE model the mixed layer depth was taken from the Hadley product using the density criteria as above.

Integrated PAR Calculations

Depth integrated PAR was calculated using the PAR from the merged GLOB colour product, K_d (λ490) from OC-CCI (to calculate the depth of the euphotic zone) and MLD from the Hadley product.

Statistical Analysis

Statistical comparisons between groups were made using the student's t-test following confirmation of equal variance. Linear regressions were performed using Ordinary Least Squares. Decadal trends from satellite NPP and integrated PAR data were calculated by first excluding any pixel whose time series had less than 50% of the data available. Before linear regressions were performed on the trends, the data were first tested for a normal distribution. If the data were

6

normally distributed then linear regressions were performed using the Sci-Kit (*75*) Huber-Regressor (ε = 1.35). If the data were not normally distributed, then linear regressions were performed using the non-parametric Mann-Kendall Test (*76*). Statistical significance is reported for $p<0.05$, $p<0.01$ and $p<0.001$.

References

62. J. Holte, L. D. Talley, J. Gilson, D. Roemmich, An Argo mixed layer climatology and database. *Geophysical Research Letters*. **44**, 5618–5626 (2017).

63. A. Olsen, N. Lange, R. M. Key, T. Tanhua, H. C. Bittig, A. Kozyr, M. Àlvarez, K. Azetsu-Scott, S. Becker, P. J. Brown, B. R. Carter, L. Cotrim da Cunha, R. A. Feely, S. van Heuven, M. Hoppema, M. Ishii, E. Jeansson, S. Jutterström, C. S. Landa, S. K. Lauvset, P. Michaelis, A. Murata, F. F. Pérez, B. Pfeil, C. Schirnick, R. Steinfeldt, T. Suzuki, B. Tilbrook, A. Velo, R. Wanninkhof, R. J. Woosley, GLODAPv2.2020 – the second update of GLODAPv2. *Earth Syst. Sci. Data Discuss.* **2020**, 1–41 (2020).

64. S. A. Good, M. J. Martin, N. A. Rayner, EN4: Quality controlled ocean temperature and salinity profiles and monthly objective analyses with uncertainty estimates. *J Geophys Res Oceans*. **118**, 6704–6716 (2013).

65. C. Schmechtig, A. Poteau, H. Claustre, F. D'Ortenzio, G. Dall'Olmo, E. Boss, Processing Bio-Argo particle backscattering at the DAC level (2015).

66. C. Roesler, J. Uitz, H. Claustre, E. Boss, X. Xing, E. Organelli, N. Briggs, A. Bricaud, C. Schmechtig, A. Poteau, F. D'Ortenzio, J. Ras, S. Drapeau, N. Haëntjens, M. Barbieux, Recommendations for obtaining unbiased chlorophyll estimates from in situ chlorophyll fluorometers: A global analysis of WET Labs ECO sensors. *Limnology and Oceanography: Methods*. **15**, 572–585 (2017).

67. G. E. Kim, M.-A. Pradal, A. Gnanadesikan, Quantifying the biological impact of surface ocean light attenuation by colored detrital matter in an ESM using a new optical parameterization. *Biogeosciences*. **12**, 5119–5132 (2015).

68. X. Xing, N. A. B. Riggs, E. M. B. Oss, H. Ervé, C. Laustre, Improved correction for non-photochemical quenching of in situ chlorophyll fluorescence based on a synchronous irradiance profile. *Optics Express*. **26**, 2111–2125 (2018).

69. C. de Boyer Montégut, G. Madec, A. S. Fischer, A. Lazar, D. Iudicone, Mixed layer depth over the global ocean: An examination of profile data and a profile-based climatology. *Journal of Geophysical Research: Oceans*. **109** (2004), doi:10.1029/2004JC002378.

70. B. S. Sackmann, M. J. Perry, C. C. Eriksen, Fluorescene quenching from Seaglider Seaglider observations of variability in daytime fluorescence quenching of chlorophyll-a in Northeastern Pacific coastal waters Fluorescence quenching from Seaglider. *Biogeosciences Discussions*. **5**, 2839–2865 (2008).

71. X. Xing, H. Claustre, S. Blain, F. D'Ortenzio, D. Antoine, J. Ras, C. Guinet, Quenching correction for in vivo chlorophyll fluorescence acquired by autonomous platforms: A case study with instrumented elephant seals in the Kerguelen region (Southern Ocean). *Limnology and Oceanography: Methods*. **10**, 483–495 (2012).

72. S. Swart, S. J. Thomalla, P. M. S. Monteiro, The seasonal cycle of mixed layer dynamics and phytoplankton biomass in the Sub-Antarctic Zone: A high-resolution glider experiment. *Journal of Marine Systems*. **147**, 103–115 (2015).

73. T. Coleman, Y. Li, An Interior Trust Region Approach for Nonlinear Minimization Subject to Bounds. *SIAM Journal on Optimization*. **6**, 418–445 (1996).

74. T. F. Coleman, Y. Li, On the convergence of interior-reflective Newton methods for nonlinear minimization subject to bounds. *Mathematical Programming*. **67**, 189–224 (1994).

75. F. Pedregosa, G. Varoquaux, A. Gramfort, V. Michel, B. Thirion, O. Grisel, M. Blondel, P. Prettenhofer, R. Weiss, V. Dubourg, J. Vanderplas, A. Passos, D. Cournapeau, M. Brucher, M.

Perrot, É. Duchesnay, Scikit-learn: Machine Learning in Python. *Journal of machine learning research*. **85**, 2825–2830 (2011).

76. M. M. Hussain, I. Mahumd, pyMannKendall: a python package for non parametric Mann Kendall family of trends tests. *Journal of Open Source Software*. **4**, 1556 (2019).

77. A. H. Orsi, T. Whitworth, W. D. Nowlin, On the meridional extent and fronts of the Antarctic Circumpolar Current. *Deep Sea Research Part I: Oceanographic Research Papers*. **42**, 641–673 (1995).

78. A. E. Allen, J. LaRoche, U. Maheswari, M. Lommer, N. Schauer, P. J. Lopez, G. Finazzi, A. R. Fernie, C. Bowler, Whole-cell response of the pennate diatom Phaeodactylum tricornutum to iron starvation. *Proceedings of the National Academy of Sciences*. **105**, 10438–10443 (2008).

79. A. Pankowski, A. McMinn, Iron availability regulates growth, photosynthesis, and production of ferredoxin and flavodoxin in Antarctic sea ice diatoms . *Aquatic Biology*. **4**, 273–288 (2009).

80. A.-C. C. Alderkamp, G. Kulk, A. G. J. Buma, R. J. W. Visser, G. L. Van Dijken, M. M. Mills, K. R. Arrigo, The Effect of Iron Limitation on the Photophysiology of Phaeocystis Antarctica (Prymnesiophyceae) and Fragilariopsis Cylindrus (Bacillariophyceae) under Dynamic Irradiance. *Journal of Phycology*. **48**, 45–59 (2012).

81. C. J. M. Hoppe, C. S. Hassler, C. D. Payne, P. D. Tortell, B. Rost, S. Trimborn, Iron Limitation Modulates Ocean Acidification Effects on Southern Ocean Phytoplankton Communities. *PLOS ONE*. **8**, e79890 (2013).

82. K. Petrou, S. Trimborn, B. Rost, P. J. Ralph, C. S. Hassler, The impact of iron limitation on the physiology of the Antarctic diatom Chaetoceros simplex. *Marine Biology*. **161**, 925–937 (2014).

83. S. Trimborn, S. Thoms, K. Bischof, S. Beszteri, Susceptibility of Two Southern Ocean Phytoplankton Key Species to Iron Limitation and High Light . *Frontiers in Marine Science* . **6** (2019), p. 167.

84. F. Koch, S. Beszteri, L. Harms, S. Trimborn, The impacts of iron limitation and ocean acidification on the cellular stoichiometry, photophysiology, and transcriptome of Phaeocystis antarctica. *Limnology and Oceanography*. **64**, 357–375 (2019).

85. C. Schallenberg, R. F. Strzepek, N. Schuback, L. A. Clementson, P. W. Boyd, T. W. Trull, Diel quenching of Southern Ocean phytoplankton fluorescence is related to iron limitation. *Biogeosciences*. **17**, 793–812 (2020).

86. D. Bozzato, T. Jakob, C. Wilhelm, S. Trimborn, Effects of iron limitation on carbon balance and photophysiology of the Antarctic diatom Chaetoceros cf. simplex. *Polar Biology*. **44**, 275–287 (2021).
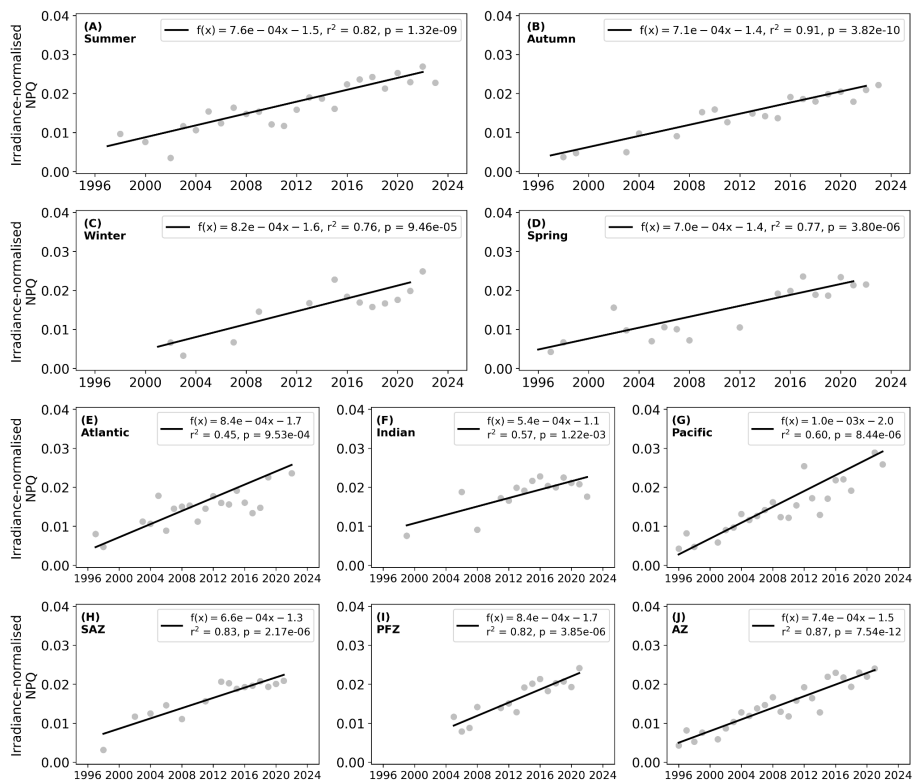
Fig. S1.

Seasonal and spatial (basin-scale and zonal) variability of the multi-decadal trends in irradiance-normalised NPQ. Ordinary Least Squares regressions of the annual means of irradiance-normalised NPQ per season for (A) Summer (December – February), (B) Autumn (March – May), (C) Winter (June – August) and (D) Spring (September – November); per ocean basin for (E) Atlantic, (F) Indian and (G) Pacific; and per frontal zone for (H) the Sub-Antarctic zone (SAZ), (I) the polar frontal zone (PFZ) and (J) the Antarctic zone (AZ). The ocean basins were defined as

12

Atlantic: 65°W to 20°E, Indian: 20°E to 145°E and Pacific: 145°E to 65°W, and the mean frontal positions were taken from Orsi et al. (*77*).
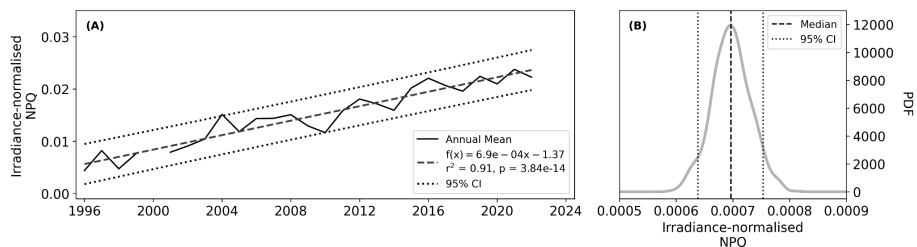
13

Fig. S2.

Multi-decadal trends in irradiance-normalised NPQ with different data resampling methods. (A) The trend in irradiance-normalised NPQ calculated from 1000 permutations, where an annual mean of irradiance-normalised NPQ was generated from 3 random profiles selected per year. Displayed is the mean with an Ordinary Least Squares (OLS) regression and 95% confidence intervals (CI). (B) Probability density function (PDF) of OLS regression results from a jackknife Monte Carlo experiment in which 75% of the 1996 – 2022 period are sub-sampled randomly, exploring the sensitivity of the annual trend calculation.
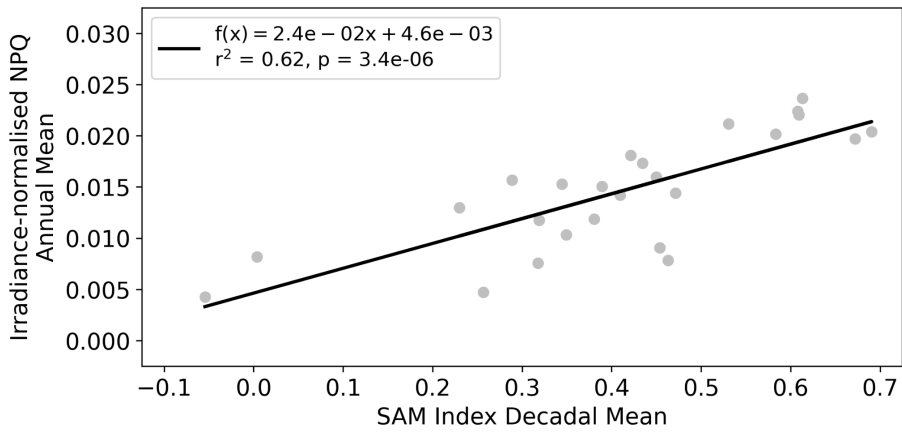
Fig. S3.

Investigating the relationship between irradiance-normalised NPQ and the dominant climate drivers. The annual mean of irradiance-normalised NPQ against a decadal rolling mean of the Southern Annular Mode (SAM) index with an Ordinary Least Squares regression for the period of 1996 - 2022.
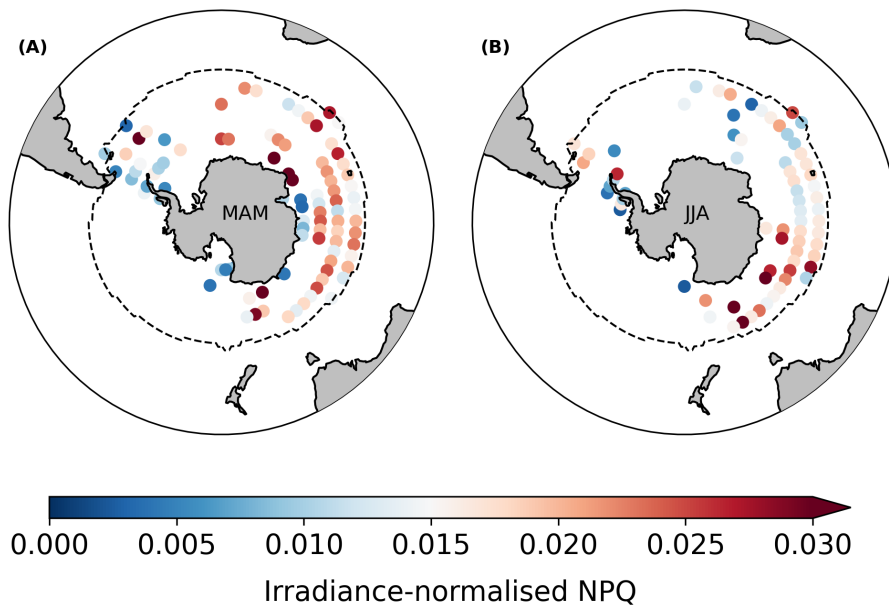
Fig. S4.

Variability of irradiance-normalised NPQ in response to seasonal Fe depletion. Maps of irradiance-normalised NPQ based on the combined BGC-Argo and ship-based profiles (1996 – 2022) for (A) Autumn (MAM: March, April and May) and (B) Winter (JJA: June, July and August) gridded to 5° × 5°. The dashed line represents the spatial extent of the Southern Ocean as defined by the subpolar and ice biomes from Fay & McKinley (*39*).
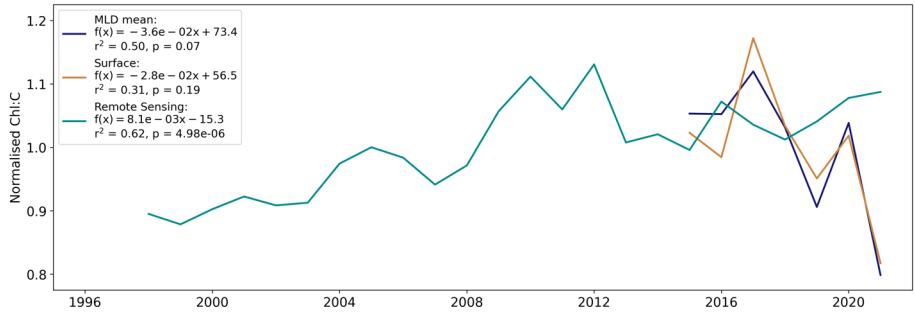
Fig. S5.

Trends of chlorophyll-a to carbon ratios from both remote sensing and BGC-Argo. Normalised annual means of chlorophyll-a to carbon ratios (Chl:C) from BGC-Argo (2015 – 2021) surface and the MLD mean and remote sensing (1998 – 2021). Normalisation was performed by dividing the data by the mean value.
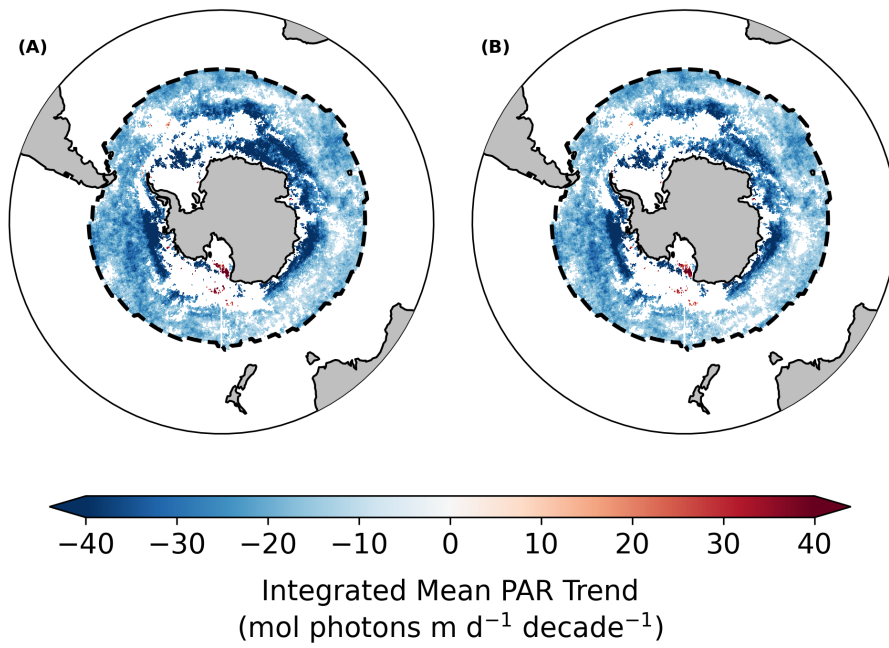
(A)

(B)

Integrated Mean PAR Trend
(mol photons m d^{-1} decade^{-1})

Fig. S6.

Changes in light availability across the Southern Ocean. Maps of decadal trends of integrated mean photosynthetically active radiation (PAR; mol photons m^{-2} d^{-1} decade^{-1}) in the (A) euphotic zone (Z$_{eu}$) and (B) mixed layer. The dashed line represents the spatial extent of the Southern Ocean as defined by the subpolar and ice biomes from Fay & McKinley (*39*).
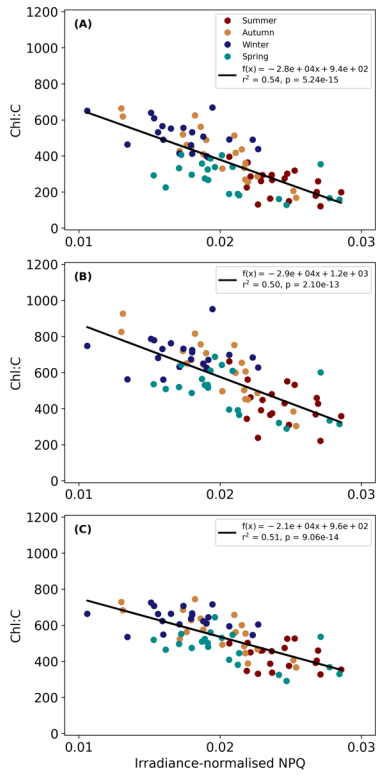
Fig. S7.

Relationships between irradiance-normalised NPQ and chlorophyll-a to carbon (Chl:C) ratios across different depth horizons, OLS regressions of monthly averaged BGC-Argo (2015 – 2021) Chl:C against irradiance-normalised NPQ from (A) surface, (B) MLD mean and (C) Z_{eu} mean.
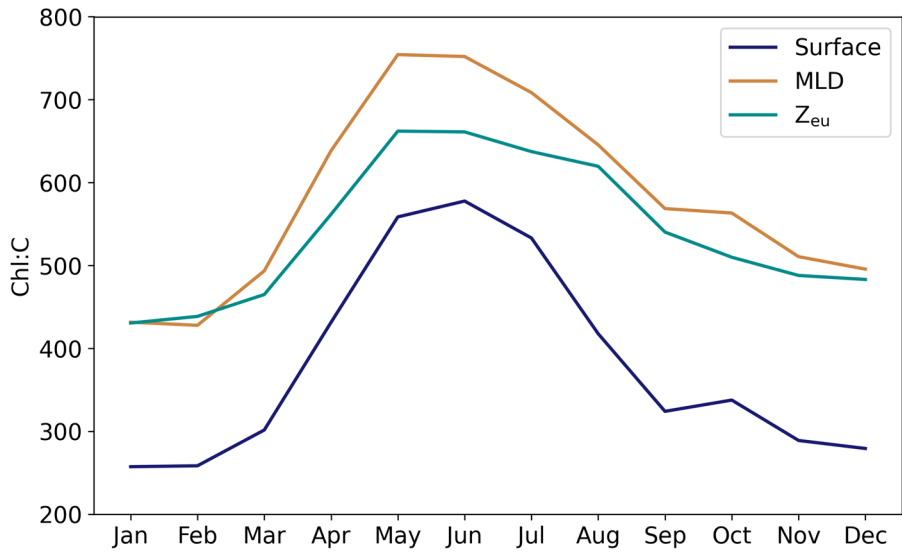
19

Fig. S8.

Seasonal cycle of chlorophyll-a to carbon (Chl:C) ratios across different depth horizons. The mean seasonal cycle (2015 – 2021) of BGC-Argo Chl:C from the surface, mean in the mixed layer (MLD) and mean in the euphotic zone (Z_{eu}).
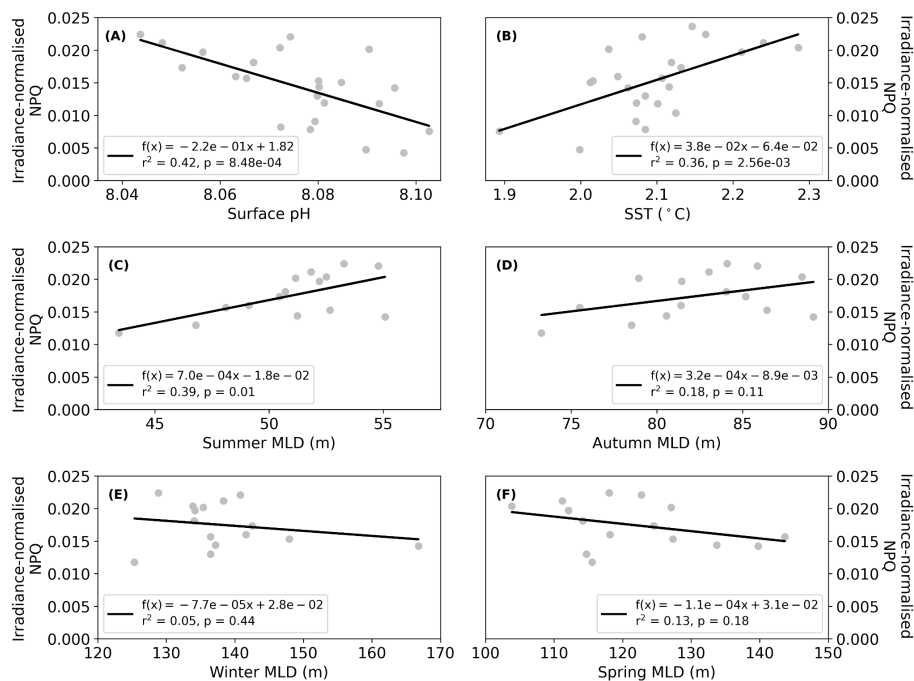
Fig. S9.

Assessing the potential drivers of irradiance-normalised NPQ. Annual means of irradiance-normalised NPQ against (A) surface pH from GLODAPv2.2021 (1996 – 2020, see Materials and Methods), (B) sea surface temperature (SST; °C) measured by GHRSST (1998 – 2021, see Materials and Methods), (C) summer (December – February) mixed layer depth (MLD), (D) autumn (March – May) MLD, (E) winter (June – August) MLD and (F) spring (September – November) MLD. MLD data were derived from core Argo (i.e not just BGC-Argo), necessitating that the analysis be restricted to between 2006 and 2021.
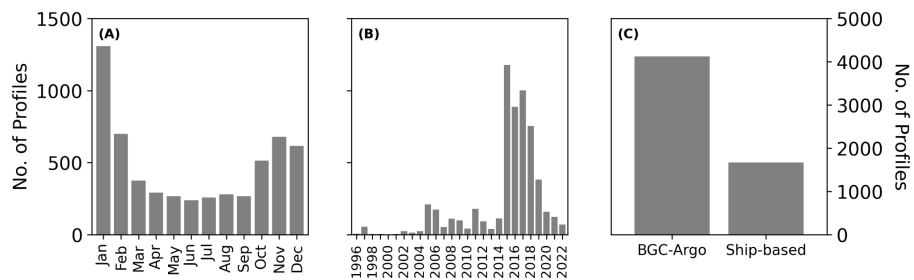
Fig. S10.

Data distribution of profiles utilised in the multi-decadal trend of irradiance-normalised NPQ. (A) Monthly distribution of profiles. (B) Annual distribution of profiles. (C) Distribution of BGC-Argo versus ship-based profiles. Please note panel (C) is scaled to the right y-axis, whereas (A) and (B) are scaled to the left y-axis.
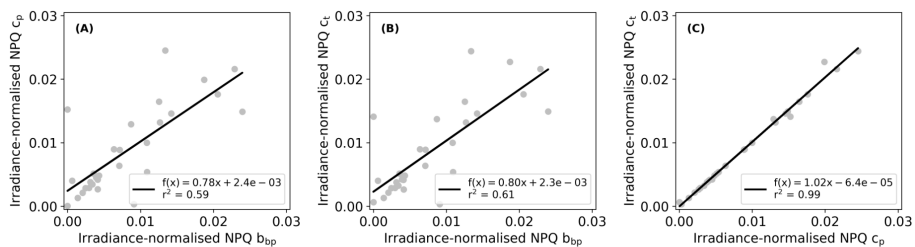
Fig. S11.

Differences in deriving irradiance-normalised NPQ with different bio-optical sensors. Comparison of irradiance-normalised NPQ derived by (A) backscatter (b_{bp}) versus beam attenuation (c_p), (B) b_{bp} versus beam transmission (c_t; converted to c_p) and (C) c_p versus c_t (c_t; converted to c_p).

Study	Species	NPQ Response to High or Low Fe	Light Level (μmol photons m^{-2} s^{-1})
Allen et al. (*78*)	P. tricornutum	Low > High	150
Pankowski & McMinn (*79*)	F. cylindrus	Low < High	70
	F. curta	Low > High	
Petrou et al. (*47*)	Natural Population SAZ	Low ≲ High	600
Alderkamp et al. (*80*)	P. antarctica	Low > High	2243
	F. cylindrus	Low > High	
Hoppe et al. (*81*)	Natural Population Weddell Sea	Low > High	40
Petrou et al. (*82*)	C. simplex	Low > High	2250
Trimborn et al. (*83*)	P. antarctica	Low ≲ High	20
			200
			500
	C. debilis	Low > High	20
			200
Koch et al. (*84*)	P. antarctica	Low > High	100
Schallenberg et al. (*85*)	Natural Population SAZ	Low > High	25 - 67% surface irradiance
Bozzato et al. (*86*)	C. simplex	Low ≲ High	100

24

Table S1.

Comparative directional response in non-photochemical quenching (NPQ) (i.e., higher >, lower <, or indeterminate ≶) between Fe deplete (Low) and Fe replete (High) conditions from laboratory culture and *in situ* experiments in the Southern Ocean under a range of light conditions. Studies where low Fe NPQ values were greater than high Fe NPQ values are shaded red, conversely studies when high Fe NPQ values were greater than low Fe NPQ values are shaded blue while studies where the responses were similar or mixed are shaded grey (*47, 78–86*).

Parameter	Slope	Intercept	R^2	F-statistic	p-value
SST	3.8×10^{-2}	-6.4×10^{-2}	0.36	11.71	8.48×10^{-4}
pH	-0.22	1.82	0.42	15.12	2.56×10^{-3}
Summer MLD	7.0×10^{-4}	1.8×10^{-2}	0.39	8.45	0.01
Autumn MLD	3.2×10^{-4}	8.9×10^{-3}	0.18	2.87	0.11
Winter MLD	-7.7×10^{-5}	2.8×10^{-2}	0.05	0.63	0.44
Spring MLD	-1.1×10^{-4}	3.1×10^{-2}	0.13	1.97	0.18

Table S2.

Ordinary Least Squares regression results of the annual mean irradiance-normalised NPQ against the annual mean of sea surface temperature (SST), the annual mean of surface pH and the annual mean seasonal mixed layer depth (MLD) of summer (December – February), autumn (March – May), winter (June – August) and spring (September – November). SST data from the GHRSST, surface pH was taken from GLODAPv2021 and MLD data were derived from core Argo data, with the analysis restricted between 2006 and 2020.

Float WMO	Program
3901496, 3901497, 3901498	BODC
3902120, 3902121, 3902124, 3902125, 6901004, 6901492, 6901493, 6901574, 6901575, 6901576, 6901578, 6901579, 6901580, 6901581, 6901582, 6901583, 6901584, 6901585, 6901650, 6901654, 6901660, 6901687, 6901689, 6902701, 6902734, 6902735, 6902736, 6902737, 6902738, 6902739, 6902740, 6902742, 6902743, 6902880, 6902905, 6903025, 6903026, 6903070, 6903128, 6903129, 6904235	CORIOLIS
5906223, 5906224,	CSIRO

Table S3.

The BGC-Argo world meteorological organisation (WMO) float number and programs used to compile the float-based data for derivation of irradiance-normalised NPQ.

Database	Cruise Identifier	Data available at:
AADC	AU0103, AU0603, AU0703, AU1121, AU1203, AU1402, AU1602, AU1603, TA1302	https://data.aad.gov.au/
BODC	AMT05, AMT06, AMT14, AMT23, AMT24, AMT25, BAS, BOFS, CONICYT, DI198, D371, JCR02, JR177, JR179, JR186, JR188, JR194, JR200, JR206, JR228, JR244, JR260, JR262, JR280, JR281, JR291, JR299, JR304, JR306, JR310, JR327, JR2003, JR2008, JR15006, JR16002, JR16004, ORCHESTRA, SO_AntEco	https://www.bodc.ac.uk/
CHCDO	096U20160108, 09AR1121_1, 09AR1203_1, 09AR20060102, 09AR20070117, 33RR20080204, 49NZ20121128, 49NZ20130106, 49NZ20170208, 49NZ20191229, 74JC20170124, 74JC20180126, 74JC20180923,	https://cchdo.ucsd.edu/

	20160129CCHSIOSEE, 20180829CCHSIO, 20210114CCHSIO	
CSIRO	IN2016_v01, IN2016_v02, IN2017_v02, IN2018_v01, IN2018_v04, IN2018_v05, IN2019_v01, IN2019_v02, IN2021_v01, SS2010_v01, SS2010_v02, SS2012_v03, SS2013_v03	https://www.marine.csiro.au/data/trawler/
MIMS	SANAE49, SANAE50, SANAE53, SANAE54, SANAE55, SANAE58, SCALE_Winter, SCALE_Spring, Winter2015, Winter2017	http://data.ocean.gov.za/pub/DATA/
BCO-DMO	CICLOPS, COPAS08, LMG0203, LMG0205, LMG0301, LMG0303, LMG0304, LMG0414, LMG0501, LMG0502, LMG0601, LMG0602, LMG0603, LMG0605, LMG0701, LMG0705, LMG0706, LMG0801,	https://www.bco-dmo.org/; https://www.marine-geo.org

LMG0802,	LMG0804,	LMG0901,
LMG0902,LMG1001,		LMG1010,
LMG1101,	LMG1110,	LMG1211,
LMG1401,	LMG1402,	LMG1501,
LMG1504,	LMG1509,	LMG1606,
LMG1701,	LMG1702,	LMG1704,
LMG1801,	LMG1810,	MV1101,
NBP9604,	NBP9701,	NBP9703,
NBP9708,	NBP9802,	NBP0101,
NBP0103,	NBP0104,	NBP0202,
NBP0204,	NBP0409,	NBP0501,
NBP0508,	NBP0601,	NBP0603,
NBP0608,	NBP0702,	NBP0709,
NBP0801,	NBP0802,	NBP0806,
NBP0808,	NBP0901,	NBP0902,
NBP1003,	NBP1005,	NBP1101,
NBP1103,	NBP1203,	NBP1207,
NBP1210,	NBP1302,	NBP1304,
NBP1305,	NBP1309,	NBP1402,
NBP1409,	NBP1503,	NBP1507,
NBP1511,	NBP1601,	NBP1603,
NBP1606,	NBP1608,	NBP1609,
NBP1701,	NBP1702,	NBP1704,

	NBP1801, RR1202, SOFEX Melville, SOFEX Revelle, SOIREE	
OBS-VLFR	SWINGS	http://www.obs-vlfr.fr/web/index.php

Table S4.

The databases and research cruises used to compile the ship-based data for derivation of irradiance-normalised NPQ.